Front. Earth Sci. 2021, 15(1): 1–11
https://doi.org/10.1007/s11707-020-0818-0

RESEARCH ARTICLE

Rapid flood inundation mapping by differencing water indices from pre- and post-flood Landsat images

Ramesh SIVANPILLAI (✉)[1], Kevin M. JACOBS[2,3], Chloe M. MATTILIO[4], Ela V. PISKORSKI[2]

1 Wyoming Geographic Information Science Center, University of Wyoming, Laramie, WY 82071, USA
2 Department of Ecosystem Science & Management, University of Wyoming, Laramie, WY 82071, USA
3 Haub School of Environment & Natural Resources, University of Wyoming, Laramie, WY 82071, USA
4 Department of Plant Sciences, University of Wyoming, Laramie, WY 82071, USA

Abstract Following flooding disasters, satellite images provide valuable information required for generating flood inundation maps. Multispectral or optical imagery can be used for generating flood maps when the inundated areas are not covered by clouds. We propose a rapid mapping method for identifying inundated areas based on the increase in the water index value between the pre- and post-flood satellite images. Values of the Normalized Difference Water Index (*NDWI*) and Modified *NDWI* (*MNDWI*) will be higher in the post-flood image for flooded areas compared to the pre-flood image. Based on a threshold value, pixels corresponding to the flooded areas can be separated from non-flooded areas. Inundation maps derived from differencing *MNDWI* values accurately captured the flooded areas. However the output image will be influenced by the choice of the pre-flood image, hence analysts have to avoid selecting pre-flood images acquired in drought or earlier flood years. Also the inundation maps generated using this method have to be overlaid on the post-flood satellite image in order to orient personnel to landscape features. Advantages of the proposed technique are that flood impacted areas can be identified rapidly, and that the pre-existing water bodies can be excluded from the inundation maps. Using pairs of other satellite data, several maps can be generated within a single flood which would enable emergency response agencies to focus on newly flooded areas.

Keywords Rapid Flood Mapping (RFM), inundation maps, Satellite data, *NDWI*, *MNDWI*

Received June 30, 2019; accepted March 8, 2020

E-mail: sivan@uwyo.edu

1 Introduction

Satellite images provide timely, critical information on areas impacted by flood inundation, landslides, wildfires, earthquakes, and other natural disasters (Joyce et al., 2009; Tomaszewski et al., 2015). For certain types of disasters, satellite and other remotely sensed (RS) images could be the only source of post-disaster data (Shaw et al., 2016). Following flooding events, rapid flood mapping (RFM) techniques are used for identifying the inundated areas and providing up-to-date information to emergency response agencies (Zhang et al., 2014; Amarnath, 2014). Information derived from the remotely sensed images (Goldberg et al., 2018) can be combined with terrain data, such as the Digital Elevation Model (DEM), for obtaining estimates of the water inundated areas (Wang et al., 2002; Gianinetto and Villa, 2007; Rosser et al., 2017; Notti et al., 2018). Imagery data collected from the Visible Infrared Imaging Radiometer Suite (VIIRS) on the NOAA-20 satellite are used for mapping the extent of flooding based on a series of algorithms that compare the initial results with reference land cover maps (Li et al., 2018a). For many flood disasters that extend over several days or weeks, the areal extent of inundated areas also changes during the event. Emergency response agencies need updated information about these changing conditions during the event for response and recovery activities.

The presence of clouds in optical or multispectral RS imagery limits their use for RFM because the information in the pixels covered by clouds and their shadows is not visible. Under these circumstances, RADAR data are used for mapping flood inundation areas (Manjusree et al., 2012) and water level changes (Perrou et al., 2018). Most RADAR data collected by satellites are expensive and have to be tasked, i.e., programmed ahead of time (Boni et al., 2016), unless they are accessed through entities such

as the International Charter on Disasters (Sivanpillai et al., 2017) or Sentinel Asia (Kaku et al., 2015). With the availability of data collected from Sentinel-1 (Attema et al., 2009), studies have documented increased use of pre- and post-flood RADAR data for mapping inundated areas (Amitrano et al., 2018, for example). However, the availability of experts needed for interpreting and generating flood maps from these data might be limited to some countries or regions of the world. Recent studies have demonstrated the utility of post-disaster data collected from social media for generating flood inundation models (Fohringer et al., 2015; Rosser et al., 2017; Li et al., 2018b). These newer techniques might not be applicable for all incidents especially where wireless communication infrastructure are damaged.

Since not all flood inundated areas are covered by clouds, RADAR data might not be necessary for inundation mapping. As flood waters continue to move downstream, images acquired over those areas may not contain clouds. When the presence of clouds over the impacted area is not an issue, multispectral imagery can be used for generating flood inundation maps. The number of satellites collecting multispectral remotely sensed (RS) data are relatively higher than those that collect RADAR data, thus increasing the chances of obtaining more post-flood imagery. In other words, when using multispectral RS data, inundation maps can be updated more frequently than when using RADAR data. Spectral imagery collected by Landsat 8 Operational Land Imager is an important source of multispectral data that can be used for inundation mapping.

Image classification techniques such as unsupervised, supervised, hybrid, or machine learning approaches are used for rapidly classifying the post-flood satellite images. These techniques utilize differences in the spectral reflectance properties of land cover features like bare ground, vegetation, built surfaces, and water. Based on the analysts' expertise in image processing software and available computing resources (hardware and software), satellite data can be rapidly processed for generating inundation maps.

Several RFM techniques rely on band ratios derived from spectral data and apply threshold values to the ratios for identifying areas (or pixels) corresponding to water (Ouma and Tateishi, 2006; Kwak et al., 2015; Kwak, 2017; Rosser et al., 2017). The Normalized Difference Water Index (*NDWI*) proposed by McFeeters (1996), and the Modified *NDWI* (*MNDWI*) proposed by Xu (2006) are two of the band ratios most widely used for mapping water surface areas. These two indices rely on the spectral values in the green and near-infrared regions of the electromagnetic (EM) spectrum for distinguishing pixels corresponding to water. *NDWI* and *MNDWI* can be computed from the satellite data that are currently available, and their values range from -1 to $+1$. In ratio images derived from *NDWI* or *MNDWI*, pixels with values >0 are labeled as water (McFeeters, 1996; Xu, 2006). Many other indices are available for mapping water bodies, but they would require spectral measurements recorded in other regions of the EM spectrum (Amarnath, 2014; Kwak et al., 2015).

Inundated area maps derived from post-flood satellite images include pre-existing waterbodies such as lakes, rivers, etc. as flooded areas (Fig. 1). The raw satellite image (left) and the flood map derived from it (right) includes the newly inundated areas and existing waterbodies, which results in overestimation of the impacted region. Utility of such map products could be limited if the flooded region had several waterbodies prior to the event. Further

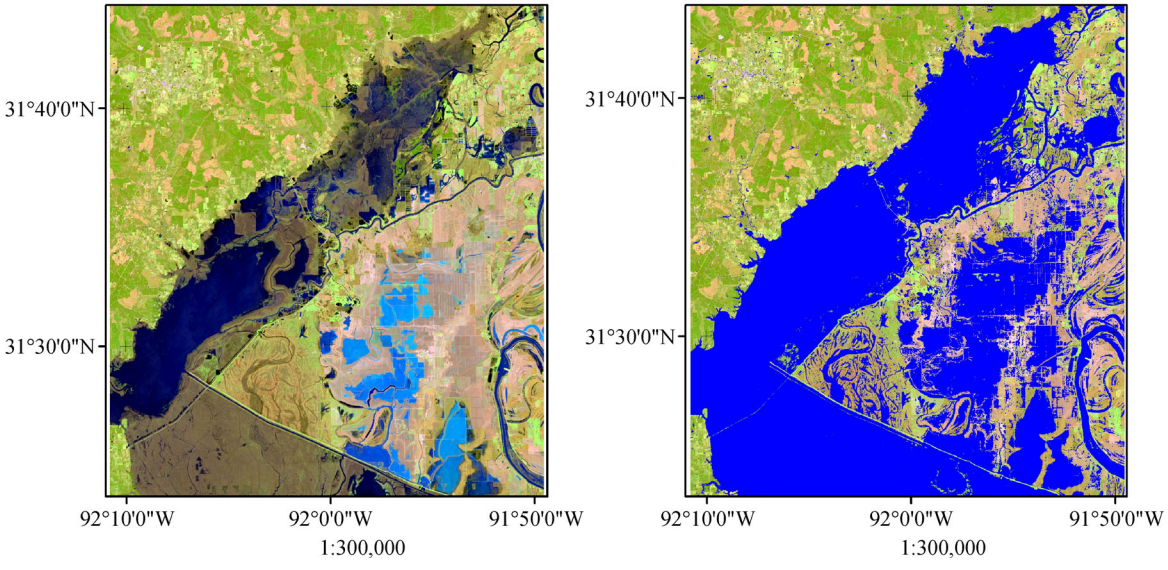

Fig. 1 Post-flood raw Landsat image (left) and classified image (right) derived from it depicts newly inundated areas (in dark blue) along with existing waterbodies such as streams, lakes and rivers resulting in overestimating the geographic extent of the impacted region.

processing might be required to separate newly inundated areas, resulting in additional delays in getting the information to emergency response agencies. Therefore, new RFM techniques focusing on mapping newly inundated areas are needed

In this paper, we describe a technique that identifies newly inundated areas based on the differences in the *NDWI* or *MNDWI* values in the pre- and post-flood images. This technique is computationally straight forward and requires an analyst to iteratively adjust and arrive at a threshold value that will adequately capture the newly inundated areas based on the changes in these two images. Some of the steps needed to generate the inundation map can be automated thus reducing the overall processing time so products can be rapidly delivered to emergency response agencies. The extent of inundated areas could change within a single flood event, and this method could be used to capture those changing conditions using several pairs of pre- and post-flood multispectral images.

2 Materials

Images representing a range of flood conditions in urban, rural, bare ground, marshes, and agricultural areas were included in this study. Flooding events were identified from the Hazards Data Distribution System (HDDS) website. HDDS contains the list of imagery and derived products provided for numerous disasters that have occurred throughout the globe. After identifying study sites (Fig. 2) and satellite images used for that event (Table 1), five pairs of pre- and post-flood Landsat images (Table 2) were downloaded from EarthExplorer which is maintained by the US Geological Survey (USGS).

Table 1 Flood events identified from the Hazards Data Distribution System website

Study area	Event ID	Event name
Arkansas	201603	Flood_Southern_US
Colorado	201309	Floods_CO
Indiana	201512	Flood_Midwest_US
Kentucky	201104	Floods_Central_US
Louisiana	201603	Flood_Southern_US

Images acquired by Landsat 5 Thematic mapper (TM5) and Landsat 8 Operational Land Imager (OLI8) sensors were included in this study. Acquisition dates of all images and sensor types are listed in Table 2. Flooded areas in the selected images included both clear and turbid water, with inundation occurring in open as well as vegetated areas.

3 Methods

3.1 Inundation maps

Individual bands of each Landsat image were stacked, and subsets were generated corresponding to the inundated areas. *NDWI* values for the Landsat TM5 and OLI8 images were computed using Eq. (1).

$$NDWI = [\text{Green} - \text{NearIR1}/[\text{Green} + \text{NearIR1}]. \quad (1)$$

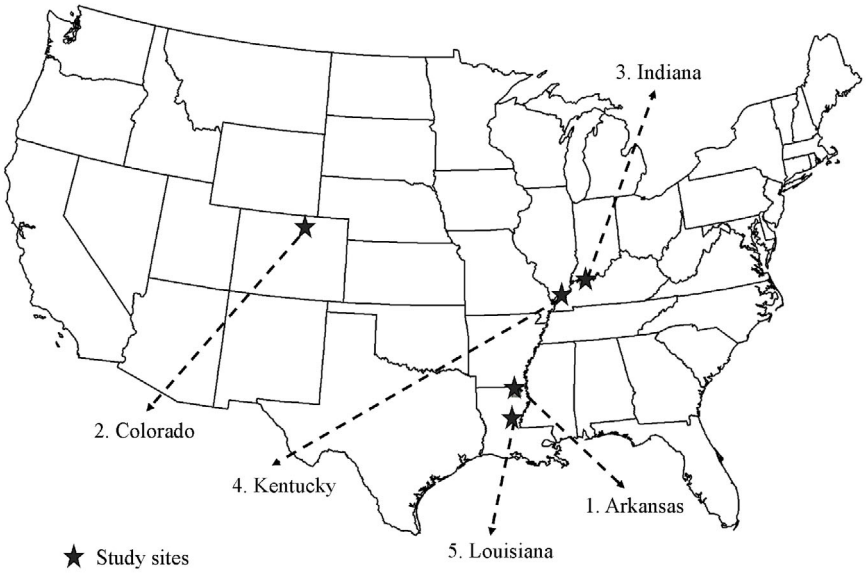

Fig. 2 Location of five study sites in the continental US.

Table 2 Details of the Landsat 5 Thematic Mapper (TM5) and Landsat 8 Operational Land Imager (OLI8) images used for mapping the flooded areas

Study area	Path/Row	Pre-flood		Post-flood	
		Sensor	Data	Sensor	Data
Arkansas	2337	OLI8	20140331	OLI8	20160320
Colorado	3432	TM5	20100925	OLI8	20130917
Indiana	2134	TM5	20110104	OLI8	20160102
Kentucky	2234	TM5	20100414	TM5	20110503
Louisiana	2338	OLI8	20140314	OLI8	20160320

Notes: 1) Spatial or pixel resolution of TM5 and OLI8 data are 30 m × 30 m, 2) Radiometric resolution of TM5 and OLI8 data are 8 and 12 bits respectively, and 3) More details on the Landsat program can be obtained from the USGS Website.

For Landsat TM5, the Green region was band 2 (0.52–0.60 μm), and the Near Infrared 1 region was band 4 (0.76–0.90 μm). For Landsat OLI8, the Green region is band 3 (0.53–0.59 μm), and the Near Infrared 1 region is band 5 (0.64–0.67 μm).

MNDWI values of the pixels in each pre- and post-flood Landsat TM5 and OLI8 images were computed using Eqs. (2) and (3) respectively.

$$MNDWI_{\mathrm{TMS}} = [\mathrm{Green} - \mathrm{NearIR2}/[\mathrm{Green} + \mathrm{NearIR2}], \quad (2)$$

$$MNDWI_{\mathrm{OLIS}} = [\mathrm{Green} - \mathrm{ShortwaveIR1}] / [\mathrm{Green} + \mathrm{ShortwaveIR1}]. \quad (3)$$

For Landsat TM5, the Green region was band 2 (0.52–0.60 μm), and the Shortwave Infrared 2 region was band 5 (1.55–1.75 μm). For Landsat OLI8, the Green region is band 3 (0.53–0.59 μm), and the Shortwave IR1 region is band 6 (1.57–1.65 μm). The width of the OLI's Near Infrared region (band 6) is slightly narrower than the corresponding width for TM5.

Using the pre- and post-flood *NDWI* or *MNDWI* images, the difference between images was computed as the percent increase in their values for a given threshold value (TV) using Eq. (4) or (5).

$$\Delta NDWI_{\mathrm{TV}} = [NDWI_{\mathrm{post-flood}} - NDWI_{\mathrm{pre-flood}}]\mathrm{TV}, \quad (4)$$

$$\Delta MNDWI_{\mathrm{TV}} = [MNDWI_{\mathrm{post-flood}} - MNDWI_{\mathrm{pre-flood}}]\mathrm{TV}. \quad (5)$$

In the difference image, pixels with Δ*NDWI* values above the specified threshold value were classified as inundated or flooded areas, i.e., the wetness value increased between the pre-flood and post-flood image. An initial TV for each image pair was set at 50%. The resulting difference image, $\Delta NDWI_{50\%}$ was visually inspected with the post-flood satellite image. If the areal extent of the inundated areas was higher in the Δ*NDWI* image, the TV was raised to generate the second difference image. The TV was decreased if the areal extent of the inundated areas was smaller in the $\Delta NDWI_{50\%}$ image. The TV was changed at 15% intervals and then 5% intervals as the images came closer to matching the post-flood image. This process was iterated until the areal extent of the inundated areas in the difference image generated with a TV (TV_F) closely matched with the extent in the post-flood image. Pixels in the difference image with values above the TV_F were assigned to flooded areas (class 1) while the rest were assigned to non-flood (class 2). These steps were repeated with the pre- and post-flood *MNDWI* images to create the second flood map and were completed using *Indices* and *Image Difference* tools in ERDAS Imagine (Hexagon Geospatial, Norcross, GA).

3.2 Reference data

Reference data were generated from each pair of pre- and post-flood images. Ideally, reference data are collected either in the field or photo-interpreted from higher spatial resolution images that were acquired nearly simultaneously. Acquiring near-simultaneous high spatial resolution data corresponding to each post-flood image was not feasible for this study as even a few days of difference in acquisition dates could alter the extent of the inundated areas.

Reference data (points) were randomly placed and photo-interpreted as either WATER or LAND after displaying them in the pre- and post-flood Landsat images. To minimize bias, interpretation of water and land features in a set of Landsat images was completed by an analyst who was not associated with determining the optimal TV. These images were displayed in false-color infrared or natural color combinations and interpretation keys such as tone (color), shape, context, and association were used for determining the class membership (Avery and Berlin, 1992). If a reference data point was interpreted as 'LAND' in the pre-flood image but as 'WATER' in the post-flood image, it was labeled as flooded (class 1). Reference data points were labeled as not flooded (class 2) if they were a) interpreted as 'LAND' or 'WATER' in both pre-flood and

post-flood images, or b) as 'WATER' in the pre-flood image and 'LAND' in the post-flood image.

3.3 Accuracy assessment

Accuracy of the difference image generated with the TV_F for each flood event was calculated by comparing it to the corresponding verification data. A pixel in the difference image was deemed as correctly classified if its thematic class matched with that of the reference data point. Otherwise the pixel considered to be was incorrectly classified in the difference image. The outputs from comparing each reference data point to the pixels were summarized in the form of an error matrix. From the error matrix, the overall, producer, and user accuracies were computed. Overall accuracy (OA) is a measure of the agreement between the reference data and the pixels in the difference image, and it is calculated as the ratio of the correctly classified data points over the total number of reference points. Producer accuracy (PA) is a measure of correctness of the individual classes, while the user accuracy (UA) is a measure of reliability from a map user's perspective (Story and Congalton, 1986). A classified image with PA and UA values close to 100% indicate that individual classes in it have been mapped accurately and are also highly reliable from a user's perspective.

The kappa (K) agreement index is computed from the error matrix and incorporates both diagonal and off-diagonal elements (Congalton, 1991). The agreement index values are categorized as poor ($K < 0.00$), slight ($0.00 \leqslant K \leqslant 0.20$), fair ($0.21 \leqslant K \leqslant 0.40$), moderate ($0.41 \leqslant K \leqslant 0.60$), substantial ($0.61 \leqslant K \leqslant 0.80$), and almost perfect if $K \geqslant 0.80$ (Watson and Petrie, 2010).

4 Results

Flood images derived from Δ*MNDWI* captured the inundated areas more closely than the Δ*NDWI* derived images (Fig. 3). Δ*NDWI* derived images misclassified several non-inundated areas as flooded prior to classifying all inundated areas. Misclassification of non-inundated areas as flooded reduces the user accuracy of the resultant map. Analysts have to select a TV_F to minimize the misclassification of non-flooded areas. Attempts to include all flooded areas by lowering the threshold values resulted in misclassification of non-flooded areas. This problem was clearly evident in the Colorado image (Fig. 3). On the other hand, Δ*MNDWI* derived images had fewer instances of non-flooded areas misclassified as flooded before all inundated areas were correctly classified.

Analysts required between 25 and 55 min for generating the flood map from each pair of pre- and post-flood images (Table 3). Analysts converted the Landsat image to *NDWI* and *MNDWI* which took approximately < 3 min each. Next, by iteratively differencing each pair of images as described in Section 3.1, the analyst determined the TV_F value that closely matched the extent of inundated areas in the post-flood images (Table 3). After starting with a value of 50%, the threshold value needed for generating each flood map (TV_F) was arrived at within five attempts (Table 3). To determine the TV_F the amount of noise generated at each TV was taken into account. Noise in the output image came from individual or a few pixels meeting the TV, creating a speckled back drop on the image. If such noisy pixels appeared in the output image, the TV was increased to reduce or eliminate them. These steps were completed in an Intel™ processor computer with a Windows™ 7 operating system.

The overall accuracy and K values computed for the flood maps generated from differencing *MNDWI* images were higher than those generated from differencing *NDWI* images (Table 4). The overall accuracy values of four of the five Δ*MNDWI* images and only one of the five Δ*NDWI* images were above 90%. Similarly, the K value was higher than 0.80 for four Δ*MNDWI* images and in only one of the Δ*NDWI* images. In the flood maps derived from Δ*NDWI*, several non-flooded areas were incorrectly classified as flooded resulting in misclassified pixels.

To maximize the value of a flood map for emergency response, it is important to correctly map most, if not all the pixels corresponding to the flooded areas resulting in high PA values. In the study, the PA values for the flood class were higher in all Δ*MNDWI* derived images than the corresponding Δ*NDWI* derived images (Table 5). Differencing *MNDWI* values (PA > 90%) resulted in correctly identifying more flooded areas than differencing *NDWI* values ($74\% \leqslant PA \leqslant 87\%$). The UA values for the flood class was higher only in two Δ*MNDWI* derived images (Arkansas and Colorado) than the Δ*NDWI* derived images. In the three remaining images the Δ*MNDWI* UA values were lower by 5%. In other words, Δ*MNDWI* derived images for Indiana, Louisiana, and Kentucky misclassified some non-flooded pixels as flooded, which will result in some overestimation of flooded areas. Based on the PA and UA values, the Δ*MNDWI* correctly classified relatively more flooded areas than the corresponding Δ*NDWI*, but it also misclassified some non-flooded areas as flooded in three flooding scenarios.

The PA values associated with the non-flood class were higher in only two Δ*MNDWI* derived images (Arkansas and Colorado) compared to the Δ*NDWI* derived images. In the three remaining images the Δ*MNDWI* PA values were lower than the Δ*NDWI* by 3%–5%. The UA values for the non-flood class were higher in all five Δ*MNDWI* derived images than they were in Δ*NDWI* derived images. In other words, fewer pixels corresponding to non-flooded areas were misclassified as flooded in the Δ*MNDWI* derived images. Based on these results, the PA and UA values for the non-flood class were relatively higher in the Δ*MNDWI* images than in the corresponding Δ*NDWI* derived images.

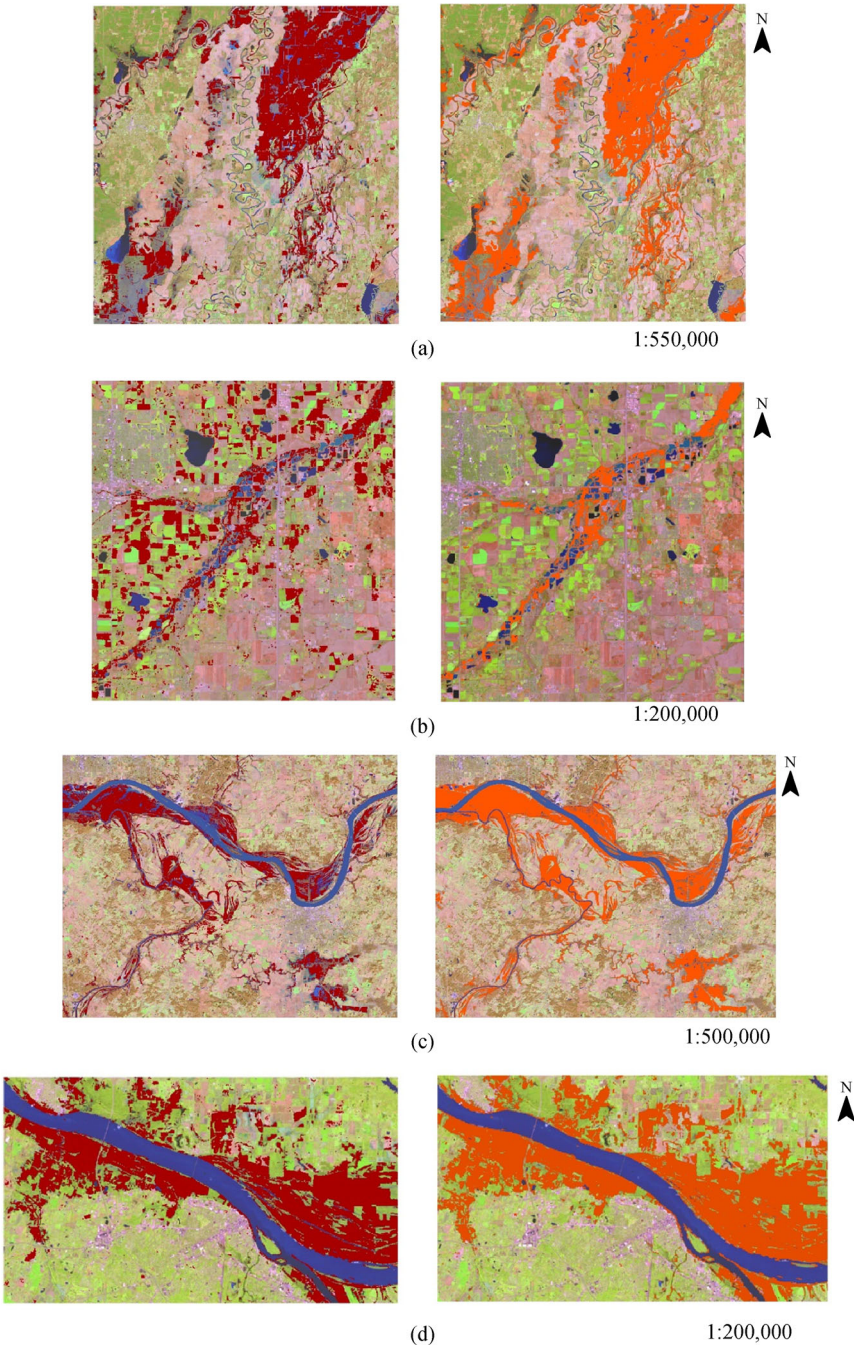

Fig. 3 Flood maps generated from Δ*NDWI* (left column) and Δ*MNDWI* (right column) for a) Arkansas, b) Colorado, c) Indiana, and d) Kentucky. Inundated areas in the difference images are highlighted in dark red (Δ*NDWI*) and bright orange (Δ*MNDWI*) colors

Based on the results from this study, the Δ*MNDWI* derived images could be more suitable for generating RF maps following a disaster. Flood maps generated by this technique exclude waterbodies such as lakes and rivers, while highlighting the flooded area (Fig. 4).

Excluding pre-existing water bodies in inundation maps will reduce the extent of impacted area in the flood maps allowing the emergency response team to focus their response activities. This will result in time saved while planning rescue missions and could possibly reduce cost by allocating resources to places that are most in need. However, the inundation maps derived from this technique have to be overlaid or superimposed on the post-flood image in order to orient the personnel to the features in the landscape.

Table 3 Threshold values (TV_F) and time required for generating rapid flood maps from differencing Normalized (*NDWI*) and Modified Normalized (*MNDWI*) Wetness Index images

Study area	Δ*NDWI*		Δ*MNDWI*	
	TV_F	Processing time	TV_F	Processing time
Arkansas	32	40	27	25
Colorado	25	20	48	35
Indiana	35	20	55	20
Kentucky	15	25	20	25
Louisiana	20	20	20	30

Table 4 Overall accuracy and kappa agreement values for the flood maps generated from differencing *NDWI* and *MNDWI* images

Study area	Overall accuracy		Kappa value	
	Δ*NDWI*	Δ*MNDWI*	Δ*NDWI*	Δ*MNDWI*
Arkansas	84.6%	93.0%	0.691	0.861
Colorado	78.0%	97.4%	0.555	0.947
Indiana	89.5%	94.3%	0.782	0.881
Louisiana	88.7%	89.7%	0.771	0.794
Kentucky	93.2%	95.2%	0.858	0.903

Table 5 Producer and user accuracy values (in percent) for the rapid flood maps generated from differencing *NDWI* and *MNDWI* images

Study area	Producer accuracy		User accuracy	
	Δ*NDWI*	Δ*MNDWI*	Δ*NDWI*	Δ*MNDWI*
Flood class				
Arkansas	75.8%	90.9%	91.5%	94.7%
Colorado	74.4%	94.2%	76.2%	100.0%
Indiana	77.6%	92.1%	91.4%	94.6%
Louisiana	83.1%	92.1%	91.4%	86.3%
Kentucky	87.1%	98.4%	96.4%	91.0%
Non flood class				
Arkansas	93.1%	95.1%	79.8%	91.5%
Colorado	81.0%	100.0%	79.4%	95.5%
Indiana	98.9%	95.8%	84.7%	93.8%
Louisiana	93.4%	87.7%	86.8%	93.0%
Kentucky	97.6%	92.6%	91.1%	98.7%

5 Discussion

Proposed RFM technique identified the flooded areas in all five study areas based on a threshold value (TV_F) that defined the cutoff for the increase in *NDWI* or *MNDWI* values. However, images derived from Δ*MNDWI* captured the newly inundated areas more accurately than the corresponding Δ*NDWI* derived images. Xu (2006) introduced *MNDWI* based on SWIR, because *NDWI* misclassified certain built-up land as water bodies. Further, *MNDWI* would have higher contrast between water and soil/vegetation than *NDWI*. Sivanpillai and Miller (2010) reported that 15 m spatial resolution ASTER data classified fewer turbid water bodies than 30 m Landsat data in the Powder River Basin. They attributed the lower accuracy of ASTER derived maps to the absence of SWIR band. In this study, the index computed with SWIR band also had higher accuracy.

Analysts were able to generate inundation maps within 45 min by determining the optimal threshold values that captured most of the newly inundated areas. Post-flood satellite images were displayed in different band combinations (true versus false colors) for determining the inundated areas. Human interpretation was necessary for

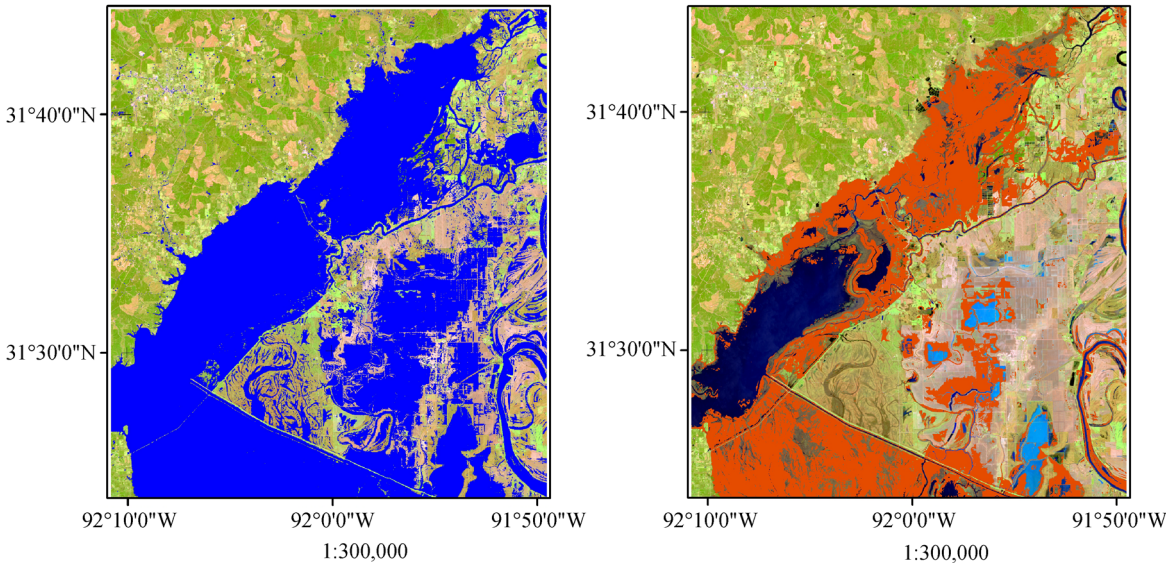

Fig. 4 Flood maps generated for the Louisiana study area from a) classifying a post-flood image using an unsupervised classification algorithm (blue color), and b) differencing a pre- and post-flood images (bright orange).

determining the trade-off between under- and over-predicting the newly inundated areas, based on omitted areas or the presence of speckles (areas with one or two pixels) in the derived products.

Another source of misclassification errors in the Δ*NDWI* derived images is due to the differences in the status of crops in the agricultural fields. In the Colorado image, many crop fields were misclassified as newly inundated areas. Examination of the input images revealed that the pre-flood image was acquired before the crops were harvested. However the post-flood image was acquired after crops in those same fields had been harvested. The Δ*NDWI* values for these fields were higher than the TV_F values, resulting in the fields being misclassified as newly flooded areas. However, the Δ*MNDWI* derived images were not impacted by the changes in the crop conditions. Satellite data collected in the SWIR regions (1.55–1.7 μm) could be useful for capturing inundated areas.

Selection of pre-flood images can influence the extent of the inundated areas in the derived products. If the pre-flood image was acquired in a dry year, the extent or area of the newly inundated areas could be high. However, if the pre-flood image was acquired in a wet year, the area could be lower. Hence the choice of pre-flood image will have a large influence on the outcome of this technique. Analysts must pay attention to land cover conditions while selecting image pairs instead of relying on anniversary date (approximately same month/week) images. In this study, harvested crop fields were a major source of misclassification in one of the test images (Colorado). Analysts must evaluate the derived products for such systematic errors, and the pre-flood image must be carefully selected prior to generating inundation images using this technique. We recommend Δ*MNDWI* derived images for RFM efforts since they were less sensitive to the changes in land cover.

Inundated areas covered by vegetation cannot be accurately mapped, since the proposed technique is based on data collected by multispectral and RADAR sensors (Pierdicca et al., 2018). Multispectral sensors measure the amount of reflected light emanating from the top of the surfaces. Under these circumstances, analysts have to combine satellite derived information with terrain data (DEM) for modeling and estimating the extent of flooding. This problem was evident in the Louisiana image with marshes and wetlands. Analysts needed additional time to determine the extent of flooding in areas covered by vegetation. Ancillary information from digital maps has to be used for identifying human settlements in areas with vegetation cover (i.e., canopy cover).

The difference images had small clusters of pixels that misclassified non-flooded areas as inundated. These speckles randomly appeared in the inundation maps and could not be eliminated by adjusting the threshold value. Applying a filter based on a minimum mapping unit can eliminate or reduce such speckles, but it creates the risk of omitting some inundated areas that are small. However, analysts could alert the response unit for such small misclassification errors while planning rescue efforts.

Mapping techniques described here can be implemented in open source software such as R or QGIS. These maps can be generated without having access to proprietary image processing software, a lack of which could be a limiting factor for emergency response agencies in some developing countries. Digital codes (or scripts) for processing these images in open source software can be developed and shared thus increasing the chances for their

adaptation. In addition, analysts can easily adapt these codes during an emergency by making minimal changes such as the name of the input variables and their location.

The time needed for generating inundation maps could be reduced if the data could be remotely processed, i.e., instead of having to download them to a local computer. Currently analysts have to download individual spectral bands from most satellite data distributors. Recently the USGS has released the Level 3 products for Landsat data series. One of the products in this suite is the dynamic surface water extent. Analysts can download these images and derive the inundation map products which would reduce some of the processing time. Moreover, with the availability of satellite data in platforms such as Google Earth Engine, analysts can derive *MNDWI* or other indices and generate the inundation products. These developments in improved data access and availability of intermediate products will result in less time needed for generating inundation maps.

While this study focused on the two commonly used indices, future studies can evaluate the suitability of other indices intended for mapping water bodies in other regions of the world. However, some of these indices require spectral information in other bands which might not be available in all satellites. RFM efforts could focus on indices that could be applied to the data collected on a majority of satellites rather than a select few.

We recognize that, presently, the 16-day revisit time of Landsat 8 satellite is a limiting factor. However, with the scheduled launch of Landsat 9 in late 2020, this revisit time will be reduced to 8 days, by combining data from both sensors. This could also increase the chances of obtaining cloud-free Landsat images for a given area. Also in this study, both pre- and post-flood images were selected from the same or similar satellite series, i.e., Landsat 5 and 8. Future studies can combine data from different satellites (Landsat pre-flood with IRS LISS III post-flood, etc.). Combining data from different satellites will pose additional challenges due to differences in their data characteristics. The spatial resolution or the spectral regions of each data could be different. However, combining data from different satellite programs would increase the chances of obtaining post-flood imagery and provide frequent updates to the emergency response agencies. However, the opportunities to combine RADAR and optical data will increase as more active sensors are launched. This will help overcome the persistent cloud cover issues for some parts of the world and result in more frequent updates to inundation conditions during the flood event. As advanced machine learning or artificial intelligence based techniques become available to analysts trained in them, the time required for human interpreter for generating such maps can be reduced.

Private companies provide data collected by their satellites to organizations such as the International Charter or Sentinel Asia as part of emergency response. Techniques proposed here have to be evaluated with these data in order to give processing insights to analysts following a disaster event. This will maximize the utility of these data during emergency response. However, these satellites do not collect data on a continuous mode, which reduces the chances of obtaining pre-flood data with identical characteristics. Therefore, data from different satellites or sensors have to be used for generating inundation maps. Future studies must extend this technique to other countries and landscapes that have mixed land use conditions with several smaller patches of inundated areas.

The RFM method proposed here can be used for generating inundation maps based on a pair of pre- and post-flood images rather than relying on existing land cover maps to isolate permanent and ephemeral water-bodies. Highlighting only the newly inundated areas, rather than including all water bodies, will help emergency management agencies with their response activities. To achieve high levels of accuracy, care must be taken while selecting the pre-flood image. Incorporating a trained analyst in the work-flow for determining the optimal threshold value reduces the classification and labeling errors.

6 Conclusions

Inundation maps derived from differencing *MNDWI* values can be used for RFM efforts of flooded areas not covered by clouds. Analysts can derive *MNDWI* images from pre- and post-satellite imagery and generate maps of the newly inundated areas within a reasonable amount of time. These maps have to be overlaid or superimposed on the post-flood satellite image in order to orient the response personnel to features in that landscape.

Inundation maps derived from differencing *NDWI* values were less accurate. However, some remote sensing satellites do not collect data in the SWIR region, and analysts have to generate inundation maps by differencing *NDWI* values.

Availability of derived products through the USGS and possibly other national agencies will further reduce the time needed to generate these inundation maps. Implementing this algorithm in platforms such as Google Earth Engine will further reduce the processing time.

Water extent in the pre-flood imagery will have a large influence on the output flood map. Hence analysts have to pay close attention to ground cover conditions in the pre-flood image.

Inundation maps generated using this differencing technique will have small speckles of misclassified pixels. Analysts have to either remove them based on a certain minimum mapping unit or alert the emergency response agency so they can exclude them while planning rescue missions.

Acknowledgements We thank the three anonymous reviewers for their valuable comments and suggestions that improved the quality of the earlier versions of the manuscript. Ms. Abigail Gettinger (University of Wyo.) provided editorial comments on the manuscript. We thank the US Geological Survey (USGS) for providing no-cost Landsat data and supporting this work under Grant/Cooperative Agreement No. G18AP00077 to the first author. The views and conclusions contained in this document are those of the authors and should not be interpreted as representing the opinions or policies of the USGS. Mention of trade names or commercial products does not constitute their endorsement by the USGS.

References

Amarnath G (2014). An algorithm for rapid flood inundation mapping from optical data using a reflectance differencing technique. J Flood Risk Manag, 7(3): 239–250

Amitrano D, Martino G D, Iodice A, Riccio D, Ruello G (2018). Unsupervised rapid flood mapping using Sentinel-1 GRD SAR images. IEEE Trans Geosci Remote Sens, 56(6): 3290–3299

Attema E, Davidson M, Snoeij P, Rommen B, Floury N (2009). Sentinel-1 mission overview. In: 2009 IEEE International Geoscience and Remote Sensing Symposium. Cape Town, South Africa

Avery T E, Berlin G L (1992). Fundamental of Remote Sensing and Airphoto Interpretation. 5th ed. New York: Macmillan Publishing Company

Boni G, Ferraris L, Pulvirenti L, Squicciarino G, Pierdicca N, Candela L, Pisani A R, Zoffoli S, Onori R, Proietti C, Pagliara P (2016). A Prototype system for flood monitoring based on flood forecast combined with COSMO-SkyMed and Sentinel-1 Data. IEEE J Sel Top Appl Earth Obs Remote Sens, 9(6): 2794–2805

Congalton R G (1991). A review of assessing the accuracy of classifications of remotely sensed data. Remote Sens Environ, 37 (1): 35–46

Fohringer J, Dransch D, Kreibich H, Schroter K (2015). Social media as an information source for rapid flood inundation mapping. Nat Hazards Earth Syst Sci, 15(12): 2725–2738

Gianinetto M, Villa P (2007). Rapid response flood assessment using minimum noise fraction and composted spline interpolation. IEEE Trans Geosci Remote Sens, 45(10): 3204–3211

Goldberg M D, Li S, Goodman S, Lindsey D, Sjoberg B, Sun D (2018). Contributions of operational satellites in monitoring the catastrophic floodwaters due to Hurricane Harvey. Remote Sens, 10(8): 1256

Kaku K, Aso N, Takiguchi F (2015). Space-based response to the 2011 great east Japan earthquake: lessons learnt from JAXA's support using earth observation satellites. Int J Disaster Risk Reduct, 12: 134–153

Kwak Y (2017). Nationwide flood monitoring for disaster risk reduction using multiple satellite data. ISPRS Int J Geoinf, 6(7): 203

Kwak Y, Shrestha B B, Yorozuya A, Sawano H (2015). Rapid damage assessment of rice crop after large-scale flood in the Cambodian floodplain using temporal spatial data. IEEE J Sel Top Appl Earth Obs Remote Sens, 8(7): 3700–3709

Li S, Sun D, Goldberg M D, Sjoberg B, Santek D, Hoffman J P, DeWeese M, Restrepo P, Lindsey S, Holloway E (2018a). Automatic near real-time flood detection using Suomi-NPP/VIIRS data. Remote Sens Environ, 204: 672–689

Li Z, Wang C, Emrich C T, Guo D (2018b). A novel approach to leveraging social media for rapid flood mapping: a case study of the 2015 South Carolina floods. Cartogr Geogr Inf Sci, 45(2): 97–110

Joyce K E, Belliss S E, Samsonov S V, McNeill S J, Glassey P J (2009). A review of the status of satellite remote sensing and image processing techniques for mapping natural hazards and disasters. Prog Phys Geogr, 33(2): 183–207

Manjusree P, Prasanna Kumar L, Bhatt C M, Rao G S, Bhanumurthy V (2012). Optimization of threshold ranges for rapid flood inundation mapping by evaluating backscatter profiles of high incidence angle SAR images. Int J Disaster Risk Sci, 3(2): 113–122

McFeeters S K (1996). The use of the Normalized Difference Water Index (*NDWI*) in the delineation of open water features. Int J Remote Sens, 17(7): 1425–1432

Notti D, Giordan D, Caló F, Pepe A, Zucca F, Galve J (2018). Potential and limitations of open satellite data for flood mapping. Remote Sens, 10(11): 1673

Ouma Y O, Tateishi R (2006). A water index for rapid mapping of shoreline changes in five East African Rift Valley lakes: an empirical analysis using Landsat TM and ETM + data. Int J Remote Sens, 27 (15): 3153–3181

Perrou T, Garioud A, Parcharidis I (2018). Use of Sentinel-1 imagery for flood management in a reservoir-regulated river basin. Front Earth Sci, 12(3): 506–520

Pierdicca N, Pulvirenti L, Chini M (2018). Flood mapping in vegetated and urban areas and other challenges: models and methods. In: Refice A, D'Addabbo A, Capolongo D, eds. Flood Monitoring through Remote Sensing. Springer Remote Sensing/Photogrammetry. Springer, Cham:135–179

Rosser J F, Leibovici D G, Jackson M J (2017). Rapid flood inundation mapping using social media, remote sensing and topographic data. Nat Hazards, 87(1): 103–120

Story M, Congalton R (1986). Accuracy assessment: a user's perspective. Photogramm Eng Remote Sensing, 52(3): 397–399

Shaw R, Izumi T, Shi P (2016). Perspectives of science and technology in disaster risk reduction of Asia. Int J Disaster Risk Sci, 7(4): 329–342

Sivanpillai R, Jones B K, Lamb R M (2017). Accessing satellite imagery for disaster response through the International Charter: lessons learned from the 2011 US Midwestern Floods. Space Policy, 42: 54–61

Sivanpillai R, Miller S N (2010). Improvements in mapping water bodies using ASTER data. Ecol Inform, 5(1): 73–78

Tomaszewski B, Judex M, Szarzynski J, Radestock C, Wirkus L (2015). Geographic information systems for disaster response: a review. J Homel Secur Emerg Manag, 12(3): 571–602

Xu H (2006). Modification of normalised difference water index (*NDWI*) to enhance open water features in remotely sensed imagery. Int J Remote Sens, 27(14): 3025–3033

Wang Y, Colby J D, Mulcahy K A (2002). An efficient method for mapping flood extent in a coastal floodplain using Landsat TM and DEM data. Int J Remote Sens, 23(18): 3681–3696

Watson P F, Petrie A (2010). Method agreement analysis: a review of correct methodology. Theriogenology, 73(9): 1167–1179

Zhang F, Zhu X, Liu D (2014). Blending MODIS and Landsat images for urban flood mapping. Int J Remote Sens, 35(9): 3237–3253

Author Biographies

Ramesh Sivanpillai received his B.Sc in physics from PSG College of Arts & Science in 1987, M.Sc in environmental studies from Cochin University of Science & Technology in 1990, M.Phil in environmental sciences from Bharathiar University, M.S. in environmental sciences from University of Wisconsin-Green Bay, and his PhD degree in forestry from Texas A&M University in 2002. He is a Senior Research Scientist at the University of Wyoming and his current research includes satellite image processing for monitoring crop fields and aquatic environments.

Kevin M. Jacobs is an undergraduate student at the University of Wyoming majoring in rangeland ecology & watershed management, and environment and natural resources.

Chloe M. Mattilio is a doctoral student in the Program in Ecology at the University of Wyoming. Her current research includes the use of unmanned aerial vehicles for mapping invasive plants.

Ela V. Piskorski is an undergraduate student at the University of Wyoming majoring in rangeland ecology & watershed management.